Long-term induced seismicity on the Mosha fault by Damavand Volcano, N-Iran, Implications on the seismic hazard of Tehran metropolis

Seyyedmaalek Momeni[1,2*], Raul Madariaga[3]

1. EPFL Geo-Energy Lab – Gaznat Chair on Geo-Energy, EPFL-ENAC-IIC-GEL, Station 18, CH-1015, Lausanne, Switzerland.

2. International Centre for Theoretical Physics (ICTP), Trieste, Italy.

3. Labratoire de Geologie, Ecole Normale Superieure, 75231 Paris Cedex 05, France.

***** Corresponding author, E-mail: maalek.momeni@gmail.com

Abstract

Seismic history of the Mosha fault, the largest and most active fault of Eastern Tehran metropolis with three documented 6.5<M<7.7 historical earthquakes, and its relation to the Damavand active Volcano, the highest mountain of the Middle East, is investigated. We infer that the seismic activity of the Central Mosha, close to the Damavand, is quite high compared to its western and eastern segments. On May 7, 2020, an Mw5.1 earthquake struck the Central Mosha, some 40 km East of Tehran, 10 km SSW of Damavand crest, and was strongly felt in Tehran. Its rupture is imaged as a patch that nucleates at the depth of 14 km and grows mostly toward up-dip and to the WNW with an average speed of 2.5 km/s that lasts for ~2.8 s. The rupture is located in a region that presented a relative seismic quiescence compared to its Eastern and Western parts, during the last 14 years, suggesting its partial locking. Early aftershocks were mainly distributed up-dip of the slip model showing a strong directivity effect. The occurrence of 1930, 1955, and

1983 earthquakes on the Central Mosha, its high microseismic activity, and the 2020 seismic sequence, strongly suggest an effect of Damavand Volcano on the seismicity of the Central Mosha. This is supported by the observed extension of a sill-like Damavand young Magma chamber until this segment of Mosha fault in tomography studies, and, by the observation of thermal areas on the Mosha fault. The existing heat raises the pore-pressure on the fault, which decreases the effective normal stress (and ease the rupture nucleation-expansion) unclamping the fault. Damavand may work as a fuse and nucleate earthquakes in which if the rupture grows toward West, will cause a strong directivity effect of low frequency seismic waves toward Tehran which currently hosts >15 million population.

1. Introduction

On May 7th, 2020, an M5.1 earthquake occurred in South-Central Alborz mountains just 4 km North of the Mosha fault (hereafter MSH), 10 km South of Damavand Volcano (hereafter DMV), which is situated 45 km East of Tehran city, capital of Iran with over 15 million population. In spite of its moderate magnitude, it caused two fatalities and several injuries (IRNA news agency). The peak ground acceleration of the mainshock was measured 115 cm/s^2 at the closest station situated just 5 km South of the epicenter. In terms of mechanism, it exhibits an almost pure strike-slip faulting (Fig. 1, reported by the Iranian Seismological Center (IRSC)). This event did not produce any surface rupture.

1.1. Tectonic Settings

46 The Alborz mountain range is part of the northern boundary between Iran and Eurasia, located
47 South of the Caspian Sea (Fig. 1). It accommodates about 30% of the total 25 mm/y of
48 shortening between Arabia and Eurasia, the remaining being accommodated both by the
49 shortening of the Zagros mountains and by long strike-slip faults in Central Iran (Vernant et al.,
50 2004). The motion between Central Iran and the South Caspian basin is oblique to the belt and
51 involves roughly ~ 5 mm/y of shortening and ~ 4 mm/y of left-lateral strike-slip motion (Vernant
52 et al., 2004). This oblique motion is due to the clockwise rotation of the South Caspian basin
53 (Djamour et al., 2010).
54
55 Alborz mountains have deformed during several tectonic episodes. The first corresponds to the
56 collision of the Iranian microplate with Eurasia that occurred during the Late Triassic (i.e.,
57 Asserto, 1966; Berberian and King, 1981; Stocklin, 1974). The second was the collision of
58 Arabia with Iran that had the main contribution to the deformation of Alborz. This collision
59 either began ~12 My ago according to the thermochronology of exhumated rocks (Guest et al.,
60 2006 a, b) or before, ~20 My ago based on the sedimentary studies of Ballato et al. (2008, 2011).
61 The second episode is associated with partitioning. It may be started 10 My ago for
62 Hollingsworth et al. (2008), 5 My for Allen et al. (2003), and even younger for Ritz et al.,
63 (2006).
64
65 The mainshock occurred near the MSH, the longest fault in South-Central Alborz with a length
66 of ~175 km and a left-lateral strike-slip faulting mechanism (Fig. 1), which mostly
67 accommodates the strike-slip component of the Caspian Sea clockwise rotational relative motion

(Djamour et al., 2010). This earthquake is the only well-recorded M>5 seismic event near the MSH by the IRSC network.

MSH consists of three segments: The western MSH segment located North of Tehran strikes WNW and is parallel to the eastern segment of the sinistral-reverse Taleghan fault (Guest et al., 2006a, b). The western MSH could be part of a local partitioning system with the Taleghan fault (Guest et al., 2006 a, b) or deactivated in favor of the Taleghan fault (Nazari et al., 2009).

The central MSH strikes WNW with a length of ~80km and branches to the West to the North Tehran fault (Solaymani et al., 2011). This segment is also a left-lateral strike-slip fault that accumulated ~35 km of total displacement (Guest et al., 2006 a, b). Abbassi and Farbod (2009), however, believe that the North Tehran fault is not presently active and suggests instead that the motion occurs on several smaller faults situated southward.

The eastern segment of MSH has a WNW strike and connects to the left-lateral/normal ENE–WSW Firuzkuh fault to the East. It is situated along the Mosha valley and is almost parallel to the Sorkhe fault on its South. This segment has a left-lateral strike-slip motion and dips to the North (Allen et al., 2004; Bachmanov et al., 2004) but with a slight normal component (Ritz et al., 2006). The total sinistral offset is ~35 km (Allen et al., 2003) and the slip rate ~2 mm/y (Ritz et al., 2006). The recent GPS measurements also estimated 1-2 mm/y of left-lateral strike-slip motion on the MSH (Djamour et al., 2010).

DMV is the highest and largest volcano of the Middle-East with an altitude of 5670 m, situated just 50 km Northeast of Tehran city. It is a young, dormant strato-volcano, which is a large intraplate Quaternary composite cone of trachyandesite lava and pyroclastic deposits overlying the active fold and thrust belt of the Central Alborz Mountains. Isotope dating, geological and tomography studies have revealed that the present cone (young Damavand) has been constructed over the last 600 Ky with a dimension of ~80 km^3, a little to the South-Southwest and on an older, eroded edifice of the old Damavand (Davidson et al., 2004, Mostafanejad et al, 2011, Shomali and Shirzad, 2014). Damavand had an average uplift rate of 3 mm/y between the years 2003 to 2010 (Vajedian et al., 2015) which was almost uniformly distributed on the area proposing its sill-like magma chamber (Yazdanparast and Vosooghi, 2014). Thermal areas exist near the MSH (Eskandari et al., 2018), confirming the extension and presence of Damavand Magma chamber toward the MSH (Fig. 6).

1.2. Historical earthquakes of Mosha fault

Three M>6.5 historical earthquakes are related to the MSH (Ambraseys and Melville, 1982; Berberian, 1994; Berberian and Yeats, 1999; Tchalenko et al., 1974): The 07/06/1665 AD (M6.5) on the eastern segment, 27/03/1830 AD (IX 7.1) on its central segment, and 23/02/958 AD (X 7.7) on its western segment which is also referred partly to the Taleghan fault (Fig. 1a).

Several moderate magnitude earthquakes have also been reported after 1800 AD on the central segment of MSH near DMV: The 1802, 20/06/1811, 1815, and the 02/10/1930 AD Ms 5.2 and 24/11/1955 AD Mb 4.0 earthquakes that occurred just South of the DMV, very close to the 2020 mainshock (Fig. 4) (Berberian et al., 1993; Nazari et al., 2009).

1.3. Instrumental earthquakes of Mosha fault and region

The instrumental seismicity is widely spread in the region. The EHB catalog (Engdahl et al., 2006) locates most of the seismicity near the Mosha, Firuzkuh, Sorkhe, and Garmsar faults (Fig. 1a). While recent seismic activity recorded by the IRSC network shows a broad distribution of seismicity in the region. Figure 1b shows selected earthquakes of the region that were recorded by the IRSC network since 2006. They are located by at least five stations, have a location error of <3 km, RMS of <0.5 s, and azimuthal gap of <180°. The eastern and central segments of the MSH show more microseismic activity compared to its western segment. A seismic cluster to the East of Tehran city is mostly related to mining activities in that area. The rest of the seismicity is related to the Sorkhe, Eyvanakey, Pishva, Garmsar, Zirab-Garmsar, Firuzkuh, and Robat-Karim faults. Detailed microseismic monitoring on the MSH by a local dense seismic network confirmed its left-lateral strike-slip mechanism with an East-Southeastward oriented fault plane (Tatar et al., 2012; Fig. 4). Tatar et al. proposed an average dip of 70° to the North for this fault.

Three moderate magnitude earthquakes with strike-slip mechanisms have been inverted by Momeni, (2012) on the central and eastern segments of the MSH; two of them (#1 and #2) were located South of DMV (Fig. 1b; #1: 20/12/2006 Mw4.2, #2: 26/02/2007 Mw3.6, and #3: 24/04/2008 Mw3.6). However, there was no seismic activity reported for the western Mosha segment neither from 1900 to 1996 (Berberian et al., 1993), nor in the recent IRSC catalog (Fig. 1b).

1.4. Our goal

In this study, we first invert the local broadband displacement full waveforms of the 7 May 2020 M5.1 mainshock for its moment tensor. Then, we invert the near field strong-motion data of the mainshock recorded in the Iranian Strong Motion Network (ISMN), for the Spatio-Temporal evolution of the slip, and investigate its relation to the distribution of early aftershocks, and the seismic history of the MSH. Finally, we investigate the relation between MSH seismic activity and DMV.

2.Moment Tensor of the 7 May 2020 M5.1 mainshock

The low-frequency full waveforms of the mainshock recorded by eight Iranian broadband seismic network (BIN) stations situated at distances ranging from 84 km to 433 km (Fig. 1a) were inverted to obtain the moment tensor, assuming a point source. The BIN seismic network is maintained by the International Institute of Earthquake Engineering and Seismology (IIEES), Tehran, Iran. More distant stations were excluded from the inversion to keep the maximum possible frequencies of the displacement waves while avoiding the undesirable effects of crustal heterogeneity on the centroid location and moment tensor calculations. The moment tensor inversion was carried out using the latest version of Isola code (Sokos and Zahradnik, 2008). The mean and trend of data were removed and bandpass filtered by fourth-order Butterworth filter between 0.03- 0.08 Hz and cut from origin time for a length of 250 s. The Green's functions for the trial point source were computed using the discrete wavenumber (DWN) method (Bouchon, 2003) and the similarity between the observed and calculated waveforms measured by the Variance Reduction (VR) parameter of the Isola code. Details of the inversion procedure are explained in a paper by Momeni and Tatar (2018). We used a velocity model of the area obtained in a detailed microseismic study by Tatar et al., (2012). The trial point sources were grid

159 searched in the activate area (Fig. 2a). The centroid time was searched as well, from 2 s before to
160 4 s after the origin time with steps of 0.08 s (Fig. 2b). The best wave-form fit was obtained for a
161 point source situated at ~4 km WNW of the hypocenter reported by IRSC, at a depth of 12 km,
162 with a space-time correlation of 85%, proposing that the rupture grew mostly to the West
163 (toward Tehran city). The NW-SE striking nodal plane has a strike/dip of 291°/60° (Figs. 2, 4),
164 which is steeper than the one obtained by IRSC (52°). The centroid depth could change between
165 11 km to 16 km, with only a slight change in the waveform-fit (<2%). A total scalar seismic
166 moment of 4.8 E+16 Nm equal to Mw 5.1 was computed.
167
168 **3.Mainshock/largest Aftershock hypocenters**
169 The mainshock and largest aftershock hypocenters were relocated by visually reading the Pg and
170 Sg crustal phases travel times recorded in the IRSC network and inverting them using the
171 HYPOCENTER code (Lienert and Havskov, 1995). We used a velocity model of the area by
172 Tatar et al., (2012) and applied the station time corrections that were obtained in their study. The
173 obtained hypocenter was situated 4 km North and 2 km East of the Mosha town, at a depth of 14
174 km (Fig. 4). It is 2 km to the North, 2 km to the East, and 3 km deeper than the IRSC hypocenter.
175 For the M4.1 aftershock, the obtained hypocenter was located 2 km South and 4 km West of the
176 mainshock hypocenter and at a depth of 9 km (Fig. 4). The latter is almost 1 km northwest of the
177 IRSC reported hypocenter and is 1 km shallower than their result.
178
179 **4. Modeling the rupture process of the mainshock**
180 **4.1. Inversion Methodology**
181 To obtain the spatial and temporal evolution of the slip for the mainshock, we invert near-field
182 strong-motion displacement time-series recorded by ten three-components SSA-2 Kinemetrics

183 digital accelerometers from the Iranian National Strong Motion Network (ISMN). The stations
184 are located at distances ranging between 4 km and 60 km from the rupture area (Fig. 1b). The
185 acceleration data is integrated twice to displacements. The mean and trend of the waveforms are
186 corrected and the horizontal components are rotated to an NS/EW coordinate system. The
187 waveforms cut using a time window of 25.6 s after the respective origin time (Fig. 3d). The data
188 were band-pass filtered using a Butterworth one-pass causal filter in the frequency band 0.08-0.4
189 Hz. We observed some low-frequency noise below 0.08 Hz. Also, the upper limit of the
190 frequency band is chosen based on the resolution of the crustal velocity model and
191 simplifications assumed in the used model.
192
193 The processed data has inverted for the rupture evolution using the elliptical sub-fault
194 approximation method (i.e., Ruiz and Madariaga, 2013; Twardzik et al., 2012; Ruiz et al., 2019;
195 Momeni et al., 2019). It approximates the rupture distribution with a few elliptical patches on a
196 planar fault, and, has the advantage of reducing the number of parameters of inversion in
197 comparison to the more commonly used rectangular sub-faults parametrization. Each of the
198 elliptical slip patches is described by just nine parameters: five to define its geometry. The other
199 four parameters to describe the rupture process, which is slip amplitude, slip duration, slip
200 direction, and onset time. While this method is not suited to retrieve fine details of the rupture
201 process, it focusses on the more robust features of the source.
202
203 Proper geometry is grid-searched for the mainshock near the two nodal planes obtained in
204 section 2 (Fig 3b). One and two elliptical patch(s) were investigated to estimate the rupture
205 process. During the inversions, for each of the tested geometries, we consider a wide range of

206 source parameters (see Figures S2 to S11). The inversions were carried out using the
207 Neighborhood Algorithm (Sambridge, 1999) to search for the rupture model that fits the best the
208 strong-motion displacements. The Green's Functions were computed using AXITRA (Cotton
209 and Coutant, 1997), a program that is based on a discrete wavenumber method (Bouchon, 2003),
210 and adopting Tatar et al., (2012) velocity model. For each inversion, the hypocenter is allowed to
211 move ±1 km on the fault plane along strike and dip to allow small corrections for errors on the
212 origin time. Up to 500 iterations were applied during inversions, and each iteration had 35
213 different trial rupture models to ensure convergence (for more details see Figures S2 to S11).
214
215 **4.2 Rupture process of the Mainshock (Mw5.1)**
216 The obtained hypocenter in section-3 has used as the initiation point of rupture, and different trial
217 planar rupture geometries were tested in the inversion using one elliptical slip patch to find the
218 optimum geometry based on waveform fit to the strong-motion records. The WNW striking
219 nodal plane provides a better wave-fit of 67%, suggesting that the rupture occurred on the MSH.
220 The geometries close to the NW striking nodal plan were investigated as well, to find a rupture
221 plane that provides the best waveform-fit to the data (Fig. 3b). The preferred geometry has a
222 strike/dip = 292°/60°. This geometry is close to the general NW strike of the MSH in this area.
223 However, the dip angle is 10 degrees less than the average dip of 70° proposed by Tatar et al.,
224 (2012) for the MSH.
225
226 **4.2.1. Rupture process using one elliptical slip patch**
227 Ten final rupture models resulted from different inversions of the near field displacement
228 waveforms are evaluated (see Fig. 3a). They describe the mainshock slip using one elliptical slip

patch. These rupture models were calculated on a planar fault with a strike/dip of 292°/60°N and with the hypocenter obtained in section-3. They have a minimum wave misfit of ~33%. For all of these models, the slip extends to the West of the hypocenter with large values located at depths ranging between 13 km to 10 km. This range is within our obtained depth range for the maximum waveform correlation in the moment tensor inversion as well as the IRSC result. The rupture has a left-lateral strike-slip mechanism (rakes =14 °-18°) and does not reach the surface.

All the models had sub-shear rupture speeds between 2.1 km/s to 3.1 km/s (Vs=3.5 km/s) and almost the same duration, between 2.2 s to 2.8 s. The rise time changes between 0.01s to 0.4s. Models with higher rise times exhibit mostly higher rupture speeds, which is consistent with the results of dynamic simulations from Schmedes et al. (2010). The maximum slip changes from 3 cm to 7 cm, depending on the rupture dimension.

The inversions converge to a seismic moment release between 3.1e+16 Nm to 3.6e+16 Nm, which are smaller than the estimated scalar moment obtained by regional waveform inversion (4.8 e+16 Nm). We stress that the low-frequency noises in the strong motions limited inversion to use frequencies below 0.08 Hz. While in section 2, we use frequency ranges down to 0.03 Hz. This observation proposes that the event has released almost 1/4 of energy at relatively lower frequencies between 0.03-0.08 Hz. Among the rupture models, we find that the largest slip model provides a higher scalar seismic moment of 3.6 e+16 Nm that is closer to the moment tensor inversion result. We select model#7 as the best slip model describing the rupture process.

Our preferred source rupture model shows nucleation at the depth of ~14 km (Fig. 4). The slip mostly extends toward the shallow depths and to the west with an average speed of 2.5 km/s. The maximum slip is estimated as ~3 cm between depths ranging from 12km to 11km. The rupture lasts for ~2.8 s and releases a total scalar seismic moment of 3.6 E+16 Nm equal to Mw 5.0. That is less than the point-source moment tensor results in section 2. The maximum slip is situated 2.5 km West and ~0.5 km South of the hypocenter and at a depth of 12 km. The rupture stops at a depth of 8 km. The rupture length of ~10 km for an M5.1 event is remarkable, proposing its comfort extension.

4.2.2. Rupture process using two elliptical slip patches

When two elliptical slip patches are used in the inversion, the misfit of the kinematic rupture models reduces to a minimum value of 31% that as expected since more parameters are used. Like the rupture models with a single slip patch, the rupture models with two slip patches show that the total scalar seismic moment was released to the West of the hypocenter and at shallow depths. Meanwhile, the two slip patches show the same features (maximum slip, rupture speed, rake, rise time). We observe that compared to the wave-fit of models with a single slip patch, the models with two slip patches did not have a considerable improvement in the wave-fit. So, the model with one slip patch is enough to estimate the mainshock rupture.

5. Aftershocks and their correlation with the mainshock rupture

27 M>=2.5 aftershocks located in the IRSC network within the first 45 days after the mainshock (Fig. 4). They have location errors of <3 km, an azimuthal gap of <180°, and an RMS of < 0.5 s. They concentrated in front of the mainshock rupture direction. All of the aftershocks are at

depths between 8 km to 14 km. Tatar et al., (2012) also located most of the microseisms on the central segment of MSH and at depths between 10 km to 15 km.

The largest (M4.1) aftershock of the 2020 sequence (occurred on May 27) is located right in front of mainshock rupture, where it was arrested, suggesting that the aftershock was a continuation of the same slipped area. Its focal mechanism is almost the same as the mainshock (Fig. 4). There are two other aftershocks far from the mainshock slip: one near the DMV, and the other in the area where the 24/11/1955 earthquake occurred.

6. Seismicity along the Mosha fault from 1996

Reliable earthquake locations by the IRSC seismic network in East of Tehran started in 1996. However, the IRSC network was relatively sparse until 2005 so that there are only 47 well-located earthquakes in the distance of 5 km from the MSH (Fig. 5 a, b). The selected earthquakes have location errors of < 5km, RMS of < 0.5 s, azimuthal gaps of < 180°, and are located by at least six stations. The mentioned events mostly distributed on the Central segment of the MSH with a considerable concentration near the DMV. As the IRSC seismic network has improved from 2006, in both terms of magnitude completeness and location accuracy, 60 M>=2.5 earthquakes were located by them in the distance of 5 km from the MSH until the May 7th mainshock (Fig. 5 a, b, Table S3). This group of earthquakes has a smaller location error of <3 km, azimuthal gap of < 180°, and RMS of < 0.5 s. This seismicity is also concentrated on the Central segment of MSH, near the DMV. While, the Eastern segment also shows seismicity on its eastern termination, and the Western one is almost silent.

297 After the 2020 mainshock, 27 M>=2.5 aftershocks were located by the IRSC network, 28 of
298 them were situated in the same distance range of 5 km from the central segment of Mosha (Fig. 5
299 b, Table S4). It is evident from Figure 5 c, d that the M5.1 mainshock rupture, and its early
300 aftershocks (45 days) occurred in a part of Mosha that had a much lower seismic activity
301 compared to its neighboring segments. As the located earthquakes after 2006 have better
302 locations, we decided to compute the cumulative scalar seismic moments of the earthquakes that
303 occurred after 2006, to investigate the seismic energy release behavior along the fault. The
304 cumulative scalar seismic moment plot shows three peaks of seismic energy: two of them on the
305 East and West of the M5.1 rupture on the central segment, and one near the eastern termination
306 of the fault (Fig. 5 b, c). These peaks are mostly related to three events occurred on 20/12/2006
307 Mw4.2 (#1), 26/02/2007 Mw3.6 (#2), and 4/04/2008 Mw3.6 (#3), and their moment tensors were
308 inverted by Momeni, (2012) (Fig. 1b).
309
310 The early aftershocks were surrounded by the two peaks of cumulative scalar seismic moment
311 release of earthquakes from 2006 until the M5.1 mainshock (Fig. 5c). After the mainshock, the
312 cumulative scalar seismic moment plot shows a big peak in the mainshock slip area and its
313 related aftershocks (Fig. 5d) that has a comparable amplitude to the scalar seismic moment
314 release from the 1930 M5.2 earthquake.
315
316 **7. Discussion**
317 The seismicity of the MSH is investigated from documented historical earthquakes previous to
318 22 June 2020. Three M>=6.5 historical earthquakes cover all the MSH segments. However,
319 instrumental seismicity is relatively poor. The EHB catalog (Engdahl et al., 2006) shows three

earthquakes near the Eastern and Central segments of MSH, close to DMV. GCMT catalog shows two 5<M<5.3 earthquakes on the Central and Eastern segments of the MSH. The IRSC network earthquake catalog has improved from 2006 in term of completeness. They show 67 M>=2.5 earthquakes within a distance of 5 km from the fault before the 2020 mainshock. Most of this seismicity concentrated on the Central segment of MSH, South of the DMV. Three peaks are observable in the cumulative Scalar Seismic Moment chart of these earthquakes (Fig. 5c). Interestingly, the central peaks that are mostly related to the 2006 and 2007 earthquakes, coincide with the estimated rupture areas during the Ms 5.2 1930 and Mb 4.0 1955 earthquakes. A possible explanation is that they are late aftershocks of these earthquakes. The Western one is close to thermal areas reported by Eskandari et al. (2018). A low-velocity region has obtained Southwest of DMV that extended until the MSH down to the depth of 15 km in a tomography study by Mostafanejad et al. (2011) (Fig. S1a). The observed thermal activities in the same area are probably due to the existence of some branches of the DMV magma chambers in that area that was also suggested by Eskandari et al. (2018).

The rupture process and the fault geometry of the 7 May 2020 M5.1 Damavand earthquake was investigated by inverting both the local broadband seismic data for the moment tensor and the near-field strong-motion displacement time series for its extended rupture model. The mainshock occurred on the central segment of the MSH: It nucleated ~15 km SSW of the DMV crest and at a depth of ~14 km. The rupture estimated in an elliptical patch with a major-minor axis of 5.8 km-3.7 km. It evolves mostly toward the West and in the up-dip direction at a sub-shear speed of ~2.5 km/s for 2.8 s. The estimated geometry is ~WNW (292°) strike and ~60° dip to the North. The obtained scalar seismic moments by point-source moment tensor inversion is 4.8 e+16 Nm

343 while using extended rupture model, this value reduces to 3.6 E+16 Nm, suggesting the release
344 of ¼ of the scalar seismic moment at relatively lower frequencies between 0.03 Hz to 0.08 Hz.
345 The Fourier spectra of four strong motion data show the low-frequency content of this event
346 (Fig. S1b). This is probably the reason that it was strongly felt in Tehran city. The rupture length
347 of >10 km for an M5.1 earthquake is remarkable and suggest the easy rupture expansion on this
348 segment of MSH.
349
350 The mainshock exhibits a left-lateral strike-slip mechanism (Rake=14°) the same as the general
351 mechanism of MSH proposed by Tatar et al., (2012), a geodetic study of Djamour et al., (2010),
352 and geological-paleoseismological studies by Nazari et al., (2009) and Solaymani-Azad et al.,
353 (2011). A maximum slip of ~3 cm was estimated between depths of 12 km and 11 km. The
354 rupture stopped at a depth of 8 km.
355 The mainshock rupture and the early aftershocks occurred between the two peaks of cumulative
356 scalar seismic moments on the MSH, proposing that this part of the fault was somehow locked
357 compared to two other neighbors that experienced the 1930 and 1955 earthquakes.
358
359 The aftershocks were distributed toward the West and up-dip, consistent with the main rupture
360 direction and general orientation of the MSH. The largest aftershock with M4.1 occurred 20 days
361 after the mainshock with a left-lateral strike-slip mechanism (IRSC), the same as the mainshock.
362 Aftershocks surrounding the rupture model (Figs. 4, 5), is a consistent feature of large
363 earthquakes (see Henry and Das, 2002).
364

The 2020 seismic activity occurred at depth range between 15 km to 8 km, where Tatar et al. (2012) also detected most of the microearthquakes. This range is almost the same as the upper-crystalline layer of the velocity model obtained by Abbasi et al. (2010) for the region. This relatively thick and deep part of seismogenic layer may have the potential for the production of large earthquakes with low-frequency contents that can reach to Tehran with less damped seismic energy and affect the tall buildings.

The smooth geometry of the central segment of MSH may facilitate the rupture expansion on it. Occurrence of the 1930 (Ms 5.2), 1955 (Mb 4.0), 1983 (Mw 5.3), and 2020 (Mw 5.1) earthquakes in the South of the DMV, together with its seismic activity from 2006, suggest a strong relation between the volcanic activity of Damavand and relatively high seismicity rate of the central segment of the MSH. Also, most of the microseismic activity and larger microearthquakes was reported by Tatar et al. (2012) on the central segment of MSH, just to the South of DMV between longitudes from 51.75 E to 52.2 E, while their seismic network was well-distributed on the two other segments of MSH.

Previous studies suggested existence of hot young sill-like magma chamber of DMV in the Southwest of its current crater (i.e. Mostafanejad et al., 2011; Shomali and Shirzad, 2014; Yazdanparast and Vosooghi, 2014; Eskandari et al., 2018). While the old magma chamber of Damavand is detected toward the North-Northeast of the crater and is detected as a cooled high-velocity dike-like structure (Mostafanejad et al., 2011). The existing young magma chamber may increase the pore pressure on the left-lateral strike-slip MSH which consequently decreases the effective normal stress on it and facilitates the rupture nucleation-expansion (Fig. 6). Such

388 phenomena have been widely observed and reported mostly for Strike-slip and Normal faulting
389 mechanisms (i.e. Saar and Magna, 2003, Goebel et al., 2017, Scuderi et al., 2017, Johann et al.,
390 2018, Eaton and Schultz, 2018, Benson et al., 2020). On the other hand, such a mechanism may
391 not allow considerable accumulation of strain on this part of the MSH near DMV (i.e. Yagi et al.,
392 2016).
393
394 The 2020 M5.1 earthquake is the largest well-recorded event on the MSH after the 1983 event.
395 This segment of the MSH has experienced the 1830 IX 7.1 historical earthquake. All of the
396 evidence indicates that the 2020 M5.1 mainshock and recent seismicity of the central segment of
397 MSH are related to the existence/activity of the magma chamber of DMV. We also stress that
398 1930, 1955, and 1983 earthquakes on the South of DMV might have happened as a result of the
399 same unclamping mechanism due to the existing high pore pressure.
400 Compared to the Central segment of Mosha, the Western segment that is closer to Tehran city is
401 silent. However, GPS studies confirm its lower deformation rate (1mm/y, Djamour et al., 2010).
402 The occurrence of earthquakes like the 2012 Ahar-Varzaghan doublet (Mw 6.5 and Mw 6.3)
403 with almost no detected seismic activity in the IRSC network before the mainshock and low
404 deformation rate (i.e. Momeni et al., 2019) highlights the importance of a detailed seismic-
405 geodetic study on the Western segment of MSH that will affect the seismic hazard of that region,
406 and especially Tehran city. Also, the Eastern segment of MSH shows seismic activity which
407 highlights its importance as another potential segment of the MSH for future large earthquakes.
408
409 **8. Conclusion**

We infer that the seismicity of the central segment of the MSH in the South of DMV is excited by the existing young sill-like magma chamber of DMV between them. The eastern segment shows lower seismic activity and the western one is almost quiet. We suggest that the transferred heat by the magma chamber to the fractured area of the MSH raises the pore pressure that consequently decreases the effective normal stress on this part of the MSH and triggers the rupture nucleation-expansion. We observe two peaks of scalar seismic moment release on the two sides of the 7 May 2020 M 5.1 mainshock, suggesting its partial locking. The occurrence of several small to moderate magnitude earthquakes on this segment of MSH suggests a heterogeneous distribution of stress on it. In terms of rupture dynamics, DMV can work as a fuse and nucleate earthquakes on the MSH, for which if the rupture grows toward the West, it will cause a strong directivity effect for that earthquake toward Tehran megacity, similarly to the 7 May 2020 M 5.1 earthquake.

The western segment of Mosha that is the closest segment to Tehran metropolis may be fully locked, as it has almost no seismic activity, but GPS measurements show a deformation rate of 1 mm/y for it and a locking depth of 16 km is suggested. This segment did not rupture since the 958 AD M~7.7 Taleghan-Mosha historical earthquake.

9. Data and Resources

The earthquakes data are available through the Iranian Seismological Center (IRSC) network website (http://irsc.ut.ac.ir). The strong motion waveforms are available from the Iranian Strong Motion Network (ISMN) website (http://smd.bhrc.ac.ir). The supplementary data includes

velocity model of the area, earthquakes hypocenters information, moment tensor inversion result of section 2, and rupture inversion tests-results of section 4.

10. Acknowledgements

This research did not receive any specific grant from funding agencies in the public, commercial, or not-for-profit sectors. We thank IIEES, IRSC, and ISMN networks for providing the seismic and strong motion data. Figures plotted using Generic Mapping Tools (GMT) (http://gmt.soest.hawaii.edu/), personal codes in Matlab environment (https://www.mathworks.com), and Paraview software (https://www.paraview.org).

11. References

Abbassi, M.R. and Farbod, Y., 2009. Faulting and folding in quaternary deposit of Tehran's piedmont (Iran). Journal of Asian Earth Sciences, **34**, 522–531. https://doi.org/10.1016/j.jseaes.2008.08.001

Allen, M.B., Ghassemi, M.R., Sharabi, M. and Qoraishi, M., 2003. Accommodation of late Cenozoic oblique shortening in the Alborz Range, northern Iran. Journal of Structural Geology, **25**, 659–672. https://doi.org/10.1016/S0191-8141(02)00064-0

Allen, M., Jackson, J. and Walker, R., 2004. Late Cenozoic reorganisation of the Arabia–Eurasia collision and the comparison of short-term and long-term deformation rates. Tectonics, **23**, TC2008. doi:10.1029/2003TC001530.

Ambraseys, N.N. and Melville, C.P., 1982. A History of Persian Earthquakes, Cambridge Univ. Press.

Asserto, R., 1966. Geological map of upper Djadjurd and Lars valley, (central Alborz, Iran).

Inst. Geol. Univ. Milano, Serie G., 232. Spec. Pub.

Ballato, P., Nowaczyk, N.R., Landgraf, A., Strecker, M.R., Friedrich, A. and Tabatabaei, S.H., 2008. Tectonic control on the sedimentary facies pattern and sediment accumulation rates in the Miocene foreland basin of the Southern Alborz Mountains, Northern Iran. Tectonics **27**, TC6001. doi:10.1029/ 2008TC002278.

Ballato, P., Uba, C.E., Landgraf, A., Strecker, M.R., Sudo, M., Stockli, D.F., Friedrich, A. and Tabatabaei, S.H., 2011. Arabia–Eurasia continental collision: Insights from late Tertiary foreland-basin evolution in the Alborz Mountains, Northern Iran. Geological Society of America Bulletin **123**, 106–131. https://doi.org/10.1130/B30091.1

Bachmanov, D.M., Trifonov, V.G., Hessami, K.T., Kozhurin, A.I., Ivanova, T.P., Rogozhin, E.A., Hademi, M.C. and Jamali, F.H., 2004. Active faults in the Zagros and central Iran. Tectonophysics **380**, 221–241. https://doi.org/10.1016/j.tecto.2003.09.021

Benson, P.M., Austria, D.C., Gehne, S., Butcher, E., Harnett, C.E., Fazio, M., Rowley, P. and Tomas, R., 2020. Laboratory simulations of fluid-induced seismicity, hydraulic fracture, and fluid flow, Geomechanics for Energy and the Environment 24, 100169. https://doi.org/10.1016/j.gete.2019.100169.

Berberian, M. and King, G.C.P., 1981. Towards a paleogeography and tectonic evolution of Iran. Canadian Journal of Earth Sciences **18**, 210–265. https://doi.org/10.1139/e81-019

Berberian, M., Ghorashi, M., Arjangravesh, B. and Mohajer-Ashjaie, A., 1993. Seismotectonic and earthquake-fault hazard investigations in the great Ghazvin Region, Geological Survey of Iran, Report no. 57, 84pp (in Farsi), GSI, Tehran, Iran.

Berberian, M., 1994. Natural hazards and the first earthquake catalog of Iran, vol. 1: Historical hazards in Iran prior 1900, I.I.E.E.S. report.

478 Berberian, M., 1997. Seismic sources of the Transcaucasian historical earthquakes, in
479 Historical and Prehistorical Earthquakes in the Caucasus, pp. 233–311, eds., Giardini, S. and
480 Balassanian, S., Kluwer Academic Publishing, Dordrecht, Netherlands.
481 https://doi.org/10.1007/978-94-011-5464-2_13

482 Berberian, M. and Yeats, R.S., 1999. Patterns of historical earthquake rupture in the Iranian
483 Plateau. Bulletin of the Seismological Society of America **89**, 120–139.

484 Bouchon, M., 2003. A Review of the Discrete Wavenumber Method, 2003, Pure appl.
485 geophys. **160**, 445–465.

486 Cotton, F. and Coutant, O., 1997. Dynamic stress variations due to shear faults in a plane-
487 layered medium, Geophys. J. Int., **128**, 676–688. https://doi.org/10.1111/j.1365-
488 246X.1997.tb05328.x

489 Davidson, J., Hassanzadeh, J., Berzins, R., Stockli, D. F., Bashukooh, B., Turrin, B. and
490 Pandamouz, A., 2004. The geology of Damavand volcano, Alborz Mountains, northern
491 Iran. *GSA Bulletin*; **116** (1-2), 16–29. doi: https://doi.org/10.1130/B25344.1.

492 Djamour, Y., Vernant, P., Bayer, R., Nankali, H.R., Ritz, J.F., Hinderer, J., Hatam, Y., Luck,
493 B., Le Moigne, N., Sedighi, M. and Khorami, F., 2010. GPS and gravity constraints on
494 continental deformation in the Alborz mountain range, Iran, Geophys. J. Int, **181**, 1287-1301.
495 https://doi.org/10.1111/j.1365-246X.2010.04811.x

496 Eaton, D.W., and Schultz, R., 2018. Increased likelihood of induced seismicity in highly
497 overpressured shale formations, Geophysical Journal International, 214(1), 751–757,
498 https://doi.org/10.1093/gji/ggy167.

499 Engdahl, E.R., Jackson, J.A., Myers, S.C., Bergman, E.A., Priestley, K., 2006. Relocation and
500 assessment of seismicity in the Iran region. Geophys. J. Int. 167, 761–778.
501 https://doi.org/10.1111/j.1365-246X.2006.03127.x
502 Eskandari, A., Amini, S., De Rosa, R. and Donato, P., 2018. Nature of the magma storage
503 system beneath the Damavand volcano (N. Iran): An integrated study. S0024 4937(17)30423-1.
504 doi: 10.1016/j.lithos.2017.12.002.
505 Goebel, T.H.W., Weingarten, M., Chen, X., Haffener, J., Brodesky, E.E., 2017. The 2016
506 Mw5.1 Fairview, Oklahoma earthquakes: Evidence for long-range poroelastic triggering at >40
507 km from fluid disposal wells, Earth and Planetary Science Letters, **472**, 50-61. DOI:
508 10.1016/j.epsl.2017.05.011
509 Guest, B., Axen, G.J., Lam, P.S. and Hassanzadeh, J., 2006a. Late Cenozoic shortening in the
510 west-central Alborz Moutains, northern Iran, by combined conjugate strike–slip and thin-skinned
511 deformation. Geosphere **2**, 35–52. https://doi.org/10.1130/GES00019.1
512 Guest, B., Stockli, D.F., Grove, M., Axen, G.J., Lam, P.S. and Hassanzadeh, J., 2006b.
513 Thermal histories from the central Alborz Mountains, northern Iran: implications for the spatial
514 and temporal distribution of deformation in northern Iran. GSA Bulletin **118**, 1507–1521. https://
515 doi.org/10.1130/B25819.1
516 Henry, C., and S. Das, 2002. The Mw 8.2, 17 February 1996 Biak, Indonesia, earthquake:
517 Rupture history, aftershocks, and fault plane properties, Journal of Geophysical Research: Solid
518 Earth, **107**, 148-227, https://doi.org/10.1029/2001JB000796
519 Hollingsworth, J., Jackson, J., Walker, R. and Nazari, H., 2008. Extrusion tectonics and
520 subduction in the eastern South Caspian region since 10 Ma. Geology **36**, 763–766.
521 https://doi.org/10.1130/G30529Y.1

Johann, L., Shapiro, S.A. and Dinske, C., 2018. The surge of earthquakes in Central Oklahoma has features of reservoir-induced seismicity. Sci Rep 8, 11505. https://doi.org/10.1038/s41598-018-29883-9.

Lienert, B.R. and Havskov, J., 1995. A computer program for locating earthquakes both locally and globally, Seismol. Res. Lett., **66**, 26–36. https://doi.org/10.1785/gssrl.66.5.26

Mostafanejad A, Shomali ZH and Mottaghi AA., 2011. 3-D velocity structure of Damavand volcano, Iran, from local earthquake tomography. J Asian Earth Sci **42**, 1091–1096. doi: 10.1016/j. jseaes.2011.03.011.

Momeni, S.M., 2012. Seismicity and Seismotectonic of the Garmsar region. MSc. Thesis in Persian. International Institute of Earthquake Engineering and Seismology, pp. 132.

Momeni, S.M., Tatar, M., 2018. Mainshocks/aftershocks study of the August 2012 earthquake doublet on Ahar-Varzaghan complex fault system (NW Iran). Physics of the Earth and Planetary Interiors, **283**, 67-81. https://doi.org/10.1016/j.pepi.2018.08.001

Momeni, S.M., Aoudia, A., Tatar, M., Twardzik, C. and Madariaga, R., 2019. Kinematics of the 2012 Ahar–Varzaghan complex earthquake doublet (M_w6.5 and M_w6.3), Geophysical Journal International, **217**, 2097–2124. https://doi.org/10.1093/gji/ggz100.

Nazari, H., Ritz, J.-F., Shafei, A., Ghassemi, A., Salamati, R., Michelot, J.-L. and Massault, M., 2009. Morphological and paleoseismological analyses of the Taleghan fault, Alborz, Iran. Geophysical Journal International. **178**, 1028-1041, doi:10.1111/j1365-246x.2009.04173. x.

Ritz, J.-F., Nazari, H., A. Ghassemi, A., Salamati, R., Shafei, A., Solaymani, S. and Vernant, P., 2006. Active Transtension inside Central Alborz: a new insight of the Northern Iran–Southern Caspian Geodynamics. Geology **34**, 477–480. https://doi.org/10.1130/G22319.1

Schmedes, J., Archuleta, R.J. and Lavallee, D., 2010. Correlation of earthquake source

545 parameters inferred from dynamic rupture simulations, J. geophys. Res., **115**, B03304, doi:
546 10.1029/2009JB006689.

547 Solaymani, S., Ritz, J.-F. and Abbassi, M., 2011. Analyzing the junction between the Mosha
548 and the North Tehran active faults. Tectonophysics **497**, 1–14.

549 Shomali, Z. H. and Shirzad, T., 2014. Crustal structure of Damavand volcano, Iran, from
550 ambient noise and earthquake tomography. Journal of Seismology **19**, 191-200.
551 https://doi.org/10.1007/s10950-014-9458-8

552 Stocklin, J., 1974. Possible ancient continental margin in Iran. In: Burke, C., Drake, C.
553 (Eds.), Geology of Continental Margins. Springer-Verlag, New York, 873–877.
554 https://doi.org/10.1007/978-3-662-01141-6_64

555 Ruiz, S., and Madariaga, R., 2013. Kinematic and dynamic inversion of the 2008 northern
556 Iwate earthquake, Bull. Seismol. Soc. Am., **103**(2A), 694–708, doi: 10.1785/0120120056.

557 Ruiz, S., Ammirati, J.B., Leyton, F., Cabrera, L., Potin, B. and Madariaga, R.,2019. The
558 January 2019 (Mw 6.7) Coquimbo Earthquake: Insights from a Seismic Sequence within the
559 Nazca Plate. *Seismological Research Letters*; **90** (5): 1836–1843.
560 https://doi.org/10.1785/0220190079

561 Saar, M.O., Manga, M., 2003. Seismicity induced by seasonal groundwater recharge at Mt.
562 Hood, Oregon, Earth and Planetary Science Letters, **214**, 605-618.
563 https://doi.org/10.1016/S0012-821X(03)00418-7

564 Sambridge, M., 1999. Geophysical inversion with a neighborhood algorithm—I. Searching a
565 parameter space, Geophysical. J. Int., **138**, 479–494. https://doi.org/10.1046/j.1365-
566 246X.1999.00876.x

567 Scuderi, M.M., Collettini, C., Marone, C., 2017. Frictional stability and earthquake triggering

568 during fluid pressure stimulation of an experimental fault, Earth and Planetary Science Letters,
569 **477**, 84-96. https://doi.org/10.1016/j.epsl.2017.08.009
570 Sokos, E. and Zahradník, J., 2008. ISOLA a Fortran code and a Matlab GUI to perform
571 multiple-point source inversion of seismic data, Computers and Geosciences, **34**, 967-977.
572 https://doi.org/10.1016/j.cageo.2007.07.005
573 Tatar, M., Hatzfeld, D., Abbassi, A. and YaminiFard, F., 2012. Microseismicity and
574 seismotectonics around the Mosha fault (Central Alborz, Iran), Tectonophysics, **544–545**, 50-59.
575 https://doi.org/10.1016/j.tecto.2012.03.033
576 Tchalenko, J.S., Berberian, M., Iranmanesh, H., Bailly, M. and Arsovsky, M., 1974. Tectonic
577 framework of the Tehran region. Geological Survey of Iran, Report, no. 29.
578 https://doi.org/10.1016/0040-1951(75)90169-9
579 Twardzik, C., Madariaga, R., Das, S. and Custodio, S., 2012. Robust features of the source
580 process for the 2004 Parkfield, California, earthquake from strong-motion seismograms,
581 Geophys. J. Int., **191**, 1245–1254. https://doi.org/10.1111/j.1365-246X.2012.05653.x
582 Vernant, P., Nilforoushan, F., Hatzfeld, D., Abassi, M.R., Vigny, C., Masson, F., Nankali, H.,
583 Martinod, J., Ashtiani, M., Bayer, R., Tavakoli, F. and Chéry, J., 2004. Present-day crustal
584 deformation and plate kinematics in the Middle East constrained by GPS measurements in Iran
585 and northern Oman. Geophysical Journal International **157**, 381–398.
586 https://doi.org/10.1111/j.1365-246X.2004.02222.x
587 Yagi, Y., Okuwaki, R., Enescu, B. *et al.* Rupture process of the 2016 Kumamoto earthquake
588 in relation to the thermal structure around Aso volcano. *Earth Planet Sp,* **68,** 118 (2016). https://
589 doi.org/10.1186/s40623-016-0492-3.
590 Yazdanparast, M. and Vosooghi, B., 2014. A research on Damavand magma source model

591 using GPS data, Geomatics, Natural Hazards and Risk, **5**:1, 26-40, DOI:
592 10.1080/19475705.2013.772543.

593

594 **Figures:**

595

596

597

598

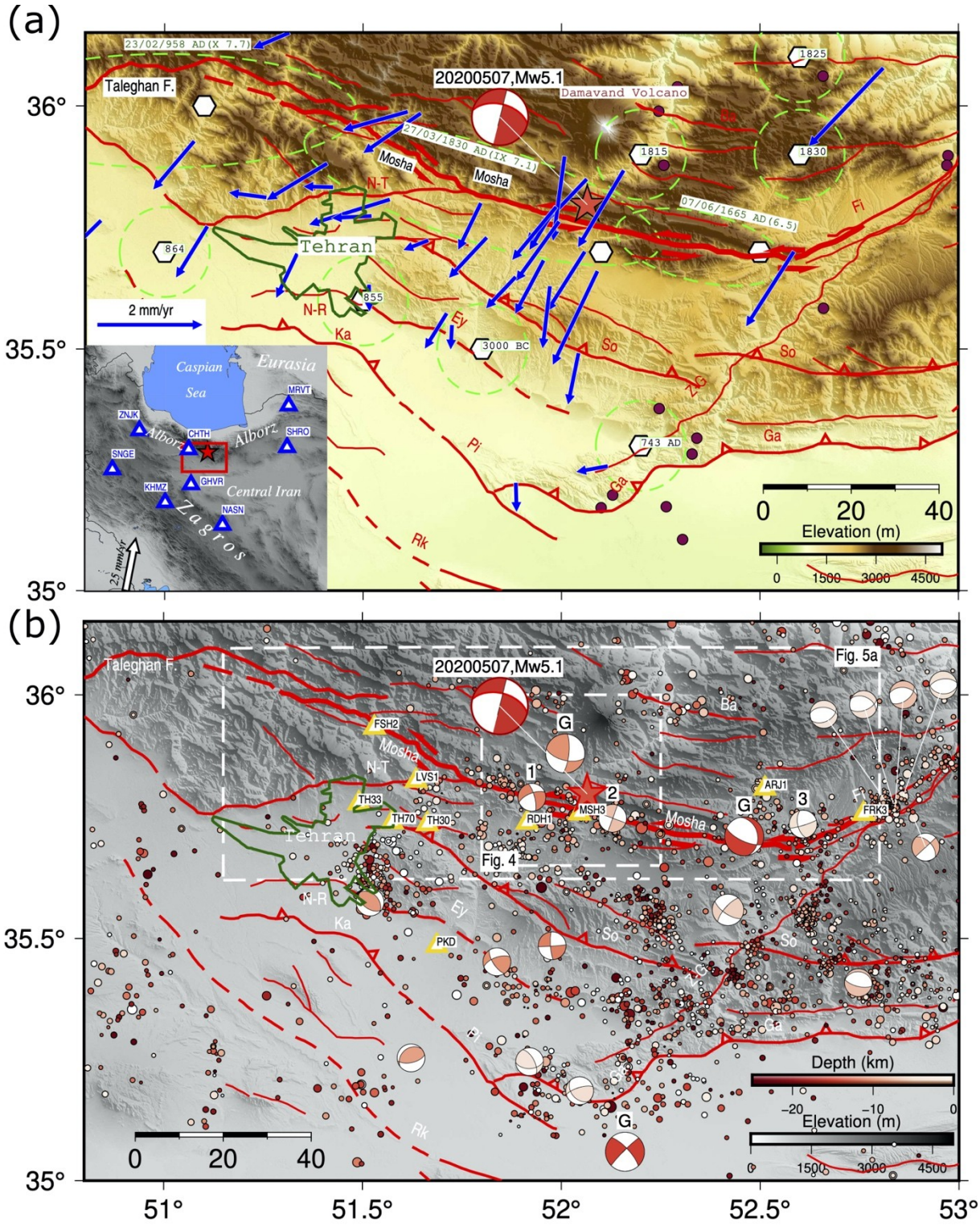

Figure 1. **a**) Seismotectonics of the study area. Red star shows the mainshock hypocenter location, and the related focal mechanism as reported by IRSC. Faults are shown with red lines.

602 Blue vectors are geodetic surface deformation rates by Djamour et al., (2010), with respect to a
603 fixed central Iran block. Blue triangles are the used station data of the Broadband national
604 Iranian Network (BIN) for moment tensor inversion (section 2). White hexagons are historical
605 earthquakes (Ambraseys and Melvile, 1982; Berberian and Yeats, 1999; Nazari et al., 2009).
606 Purple circles are instrumental earthquakes by Engdahl et al. (2006). Green ellipses show
607 affected regions by historical earthquakes. Fault names are: Ga: Garmsar; So: Sorkhe; Ey:
608 Eyvanakey; Ka: Kahrizak; Fi: Firuzkuh; Pi: Pishva; N-T: North Tehran; Ba: Baijan; Rk: Robat
609 Karim; NR: North Rey. Tehran area is in Green. MSH in red solid line. **b**) Circles: Seismicity
610 recorded by the IRSC network from 2006 until just before the M 5.1 mainshock. Colors
611 represent hypocentral depths. Faults are the same as (a). Focal mechanisms with label G are from
612 the GCMT catalog. The ones without label and those labeled 1, 2, and 3 are from small to
613 moderate magnitude earthquakes ($3.6<M<4.8$) that occurred from 2006 to 2012 in the region and
614 obtained by inverting local broadband seismic data for their moment tensors (Momeni, 2012).
615 Triangles in Gold are the Strong motion stations data of the Iranian Strong Motion Network
616 (ISMN) we used for extended rupture inversion (section 3).
617

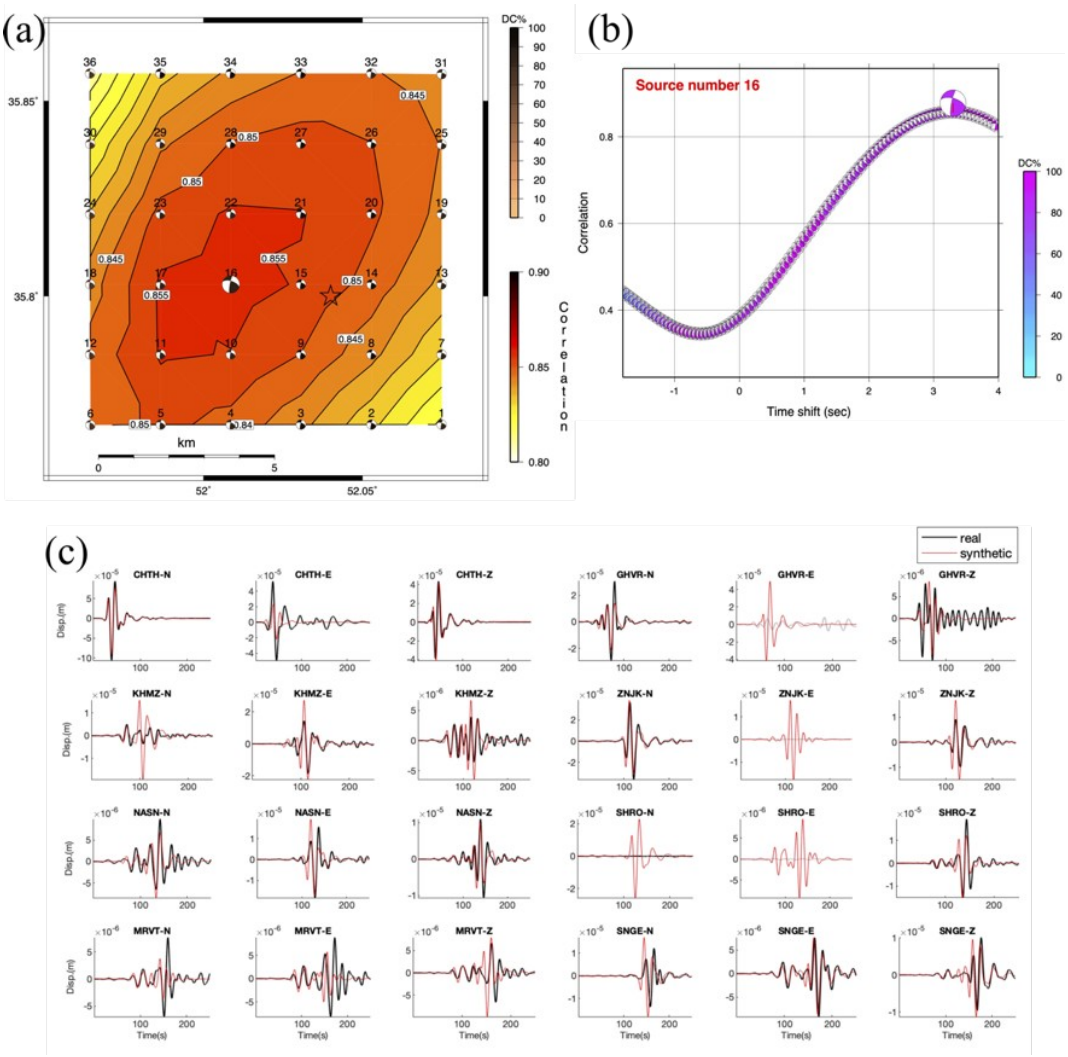

Figure 2. 3D grid search of the M5.1 mainshock centroid location-time. (**a**): Horizontal slice on the space-time correlation plot of trial centroid point sources at a depth of 12 km. The best result was obtained for source number 16 (the larger focal mechanism) with a correlation of 85% situated almost 4 km WNW of the hypocenter reported by IRSC (black star). (**b**): Centroid time correlation plot for the preferred point source #16. The best centroid time has obtained 3.3 s after the IRSC reported origin time. (**c**): Waveform-fit between the real (black) and synthetic (red) displacements for the best obtained moment tensor. Station names-components are written on the top of each sub-figure. Gray waveforms were not used in the inversion, while the related synthetics were produced by forward modeling.

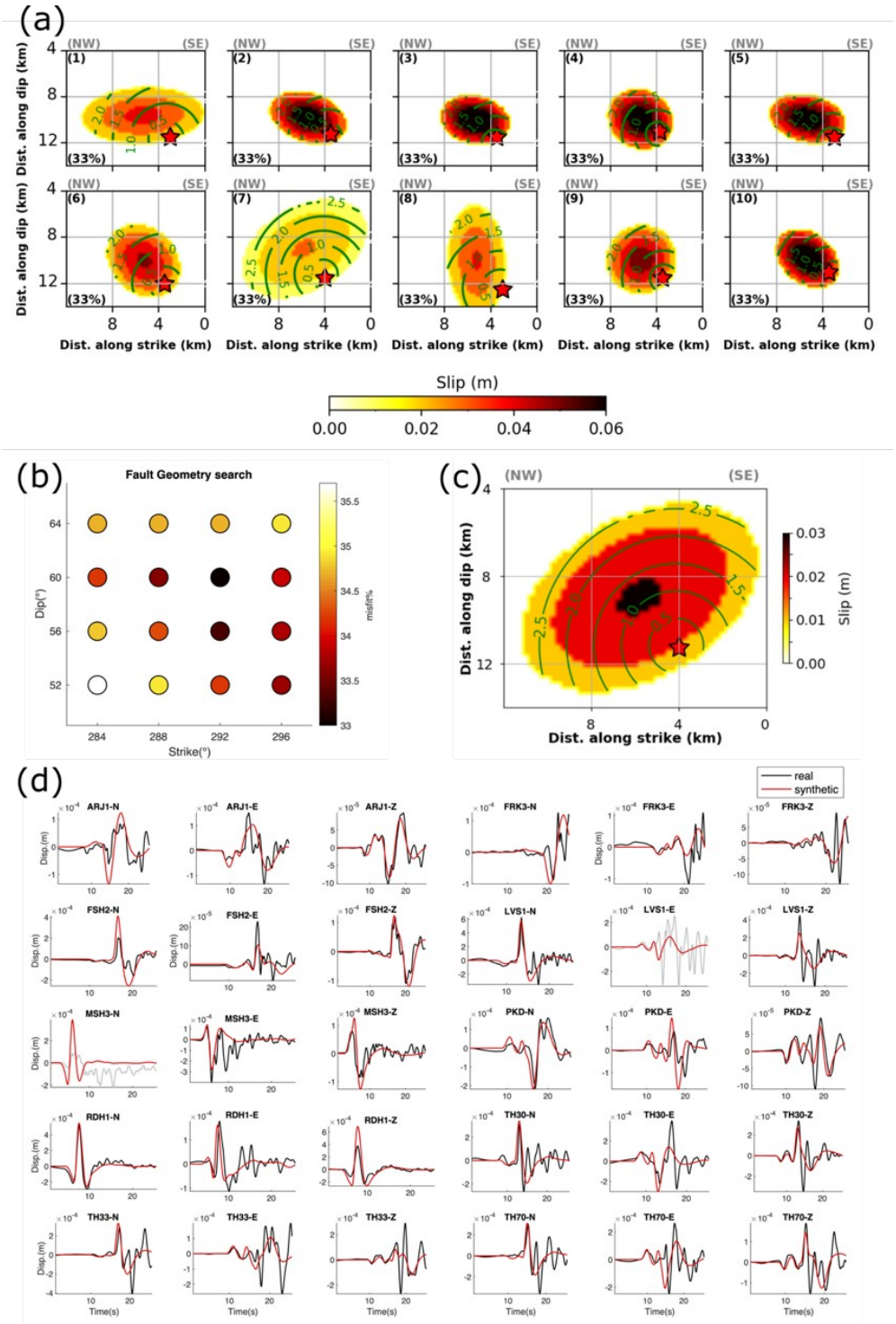

Figure 3. (a): 10 final rupture models for the mainshock obtained on the preferred geometry obtained during independent inversions, assuming different ranges for the rupture parameters.

(**b**): Grid-search of the geometry of the ruptured area. The preferred geometry has a strike/dip of 292°/60°. (**c**): The best rupture model for the mainshock. (**d**): waveform-fit of the best rupture model shown in c. Gray waveforms were not used in the inversion, their corresponding synthetic waveforms were obtained by forward-modeling.

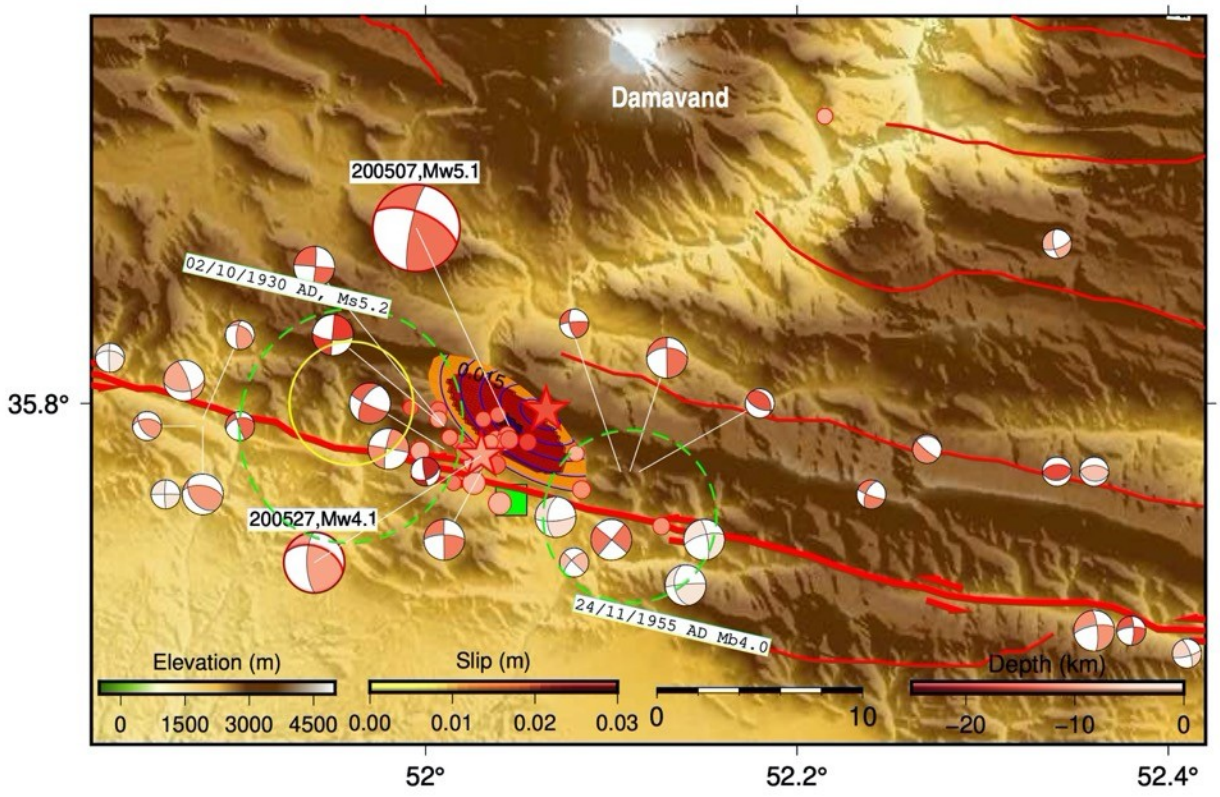

Figure 4. Correlation between mainshock rupture (colored ellipse) and aftershocks of the first 45 days (Red circles). Stars are mainshock and largest aftershock hypocenters relocated in this study (section 3). The mainshock focal mechanism is obtained in section 2. The M4.1 27/05/2020 aftershock focal mechanism is from IRSC. Inner colors represent their depths. Faults are plotted with red lines. Blue curved lines represent rupture direction. The green square is the location of Mosha town. The light-green dashed ellipses show the damage areas of the Ms 5.2 1930 and Mb 4.0 1955 earthquakes (after Berberian et al., 1993). Other focal mechanisms are from

microearthquakes on the MSH obtained by Tatar et al. (2012) from June to October 2006. Yellow circle is the observed thermal area on the MSH (after Eskandari et al., (2018).

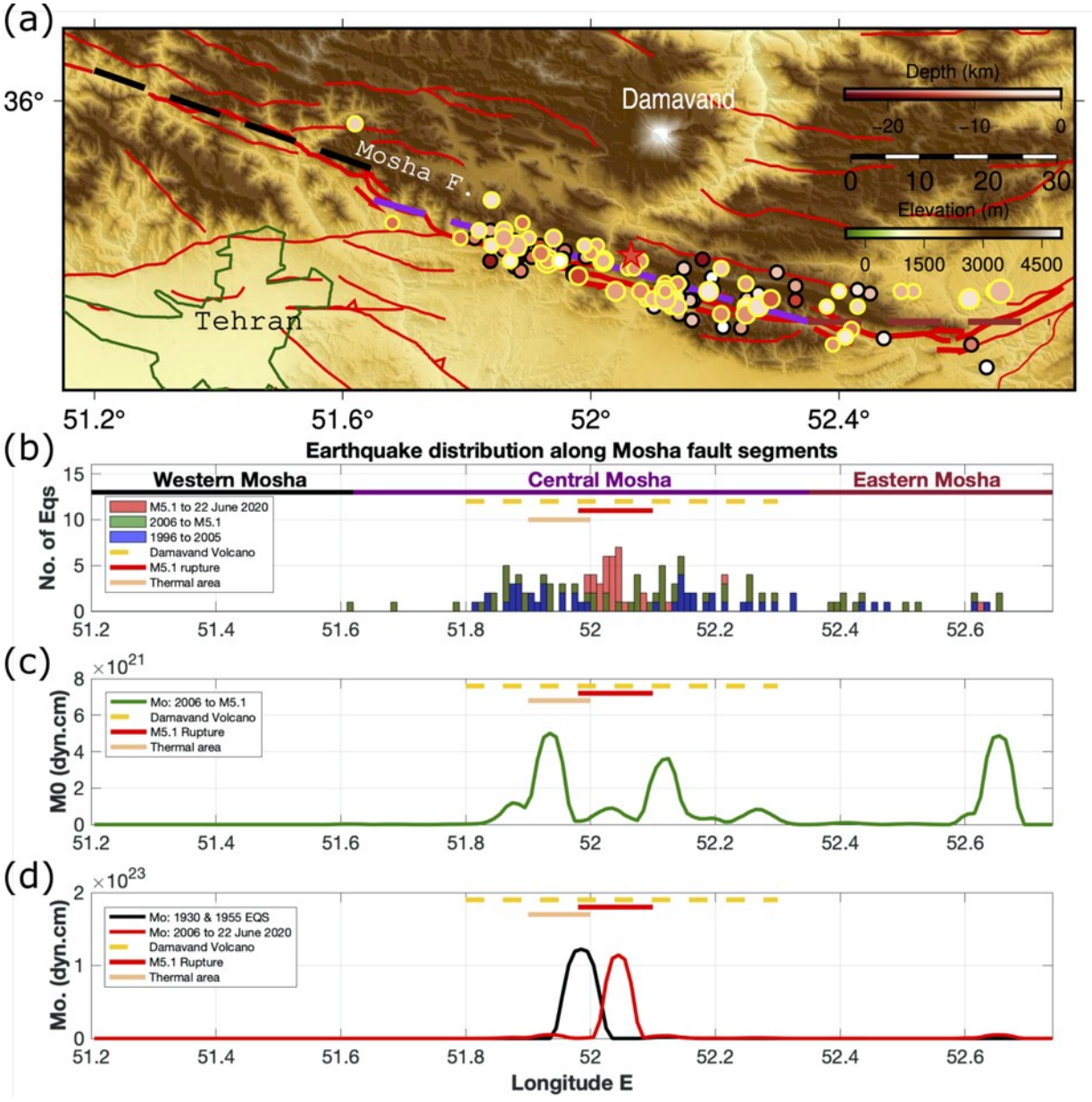

Figure 5. (**a**): Seismicity along a distance of 5 km of the MSH from 1996 until the M5.1 mainshock. Black and Yellow circles are the earthquakes from 1996 to the end of 2005, and 2006 until before the M5.1, respectively. Black, Purple, and brown dashed lines are Western, Central, and Eastern segments of the MSH, respectively. **(b)**: Histogram showing the distribution

of earthquakes along the MSH. **(c)**: Distribution of scalar seismic moments along the MSH from 2006 until before the 2020 M5.1 mainshock. **(d)**: Distribution of scalar seismic moments along MSH from 2006 until 22 June 2020, including the M5.1 mainshock and 27 M>=2.5 early aftershocks.

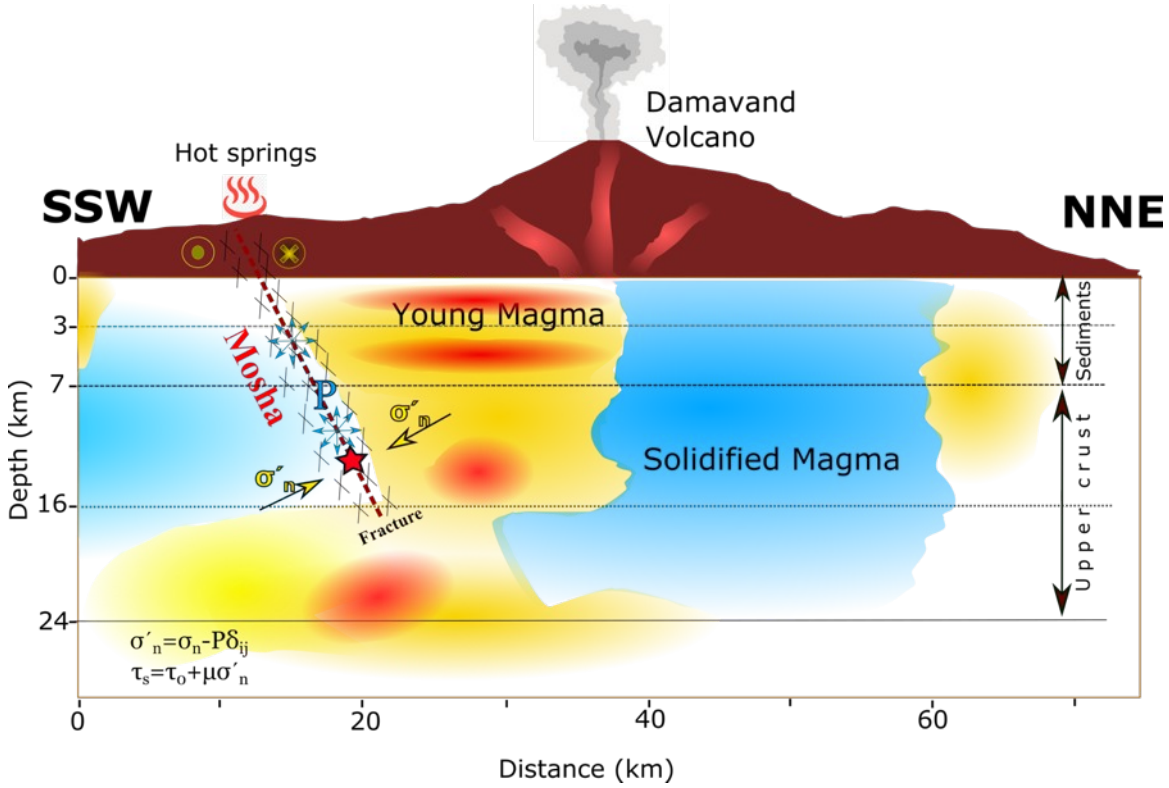

Figure 6. Schematic plot illustrating the relation between MSH and DMV. Red and Blue represent the hot and cool rocks, respectively (after Mostafanejad et al., 2011, Shomali and Shirzad, 2014, Yazdanparast and Vosooghi, 2014, Vajedian et al., 2015, Eskandari et al., 2018). Red star is the 7 May 2020 M5.1 mainshock hypocenter. Red dashed line is the MSH. Horizontal dashed lines are crustal velocity layers from Tatar et al., (2012).